Protostars and stars in the Coronet cluster: Age, evolution, and cluster structure[1]

Aurora Sicilia-Aguilar[1], Thomas Henning[1], Jouni Kainulainen[1],

Veronica Roccatagliata[2]

sicilia@mpia.de

ABSTRACT

We present new optical spectroscopy with FLAMES/VLT, near-IR imaging with HAWK-I/VLT, and 870μm mapping with APEX/LABOCA of the Coronet cluster. The optical data allow to estimate spectral types, extinction and the presence of accretion in 6 more M-type members, in addition to the 12 that we had previously studied. The submillimeter maps and near-IR data reveal the presence of nebular structures and high extinction regions, which are in some cases associated to known IR, optical, and X-ray sources. Most star formation is associated to two elongated structures crossing in the central part of the cluster. Placing all the 18 objects with known spectral types and extinction in the HR diagram suggests that the cluster is younger than previously thought (<2 Myr, and probably $\sim$0.5-1 Myr). The new age estimate is in agreement with the evolutionary status of the various protostars in the region and with its compactness (<1.3 pc across), but results in a conflict with the low disk and accretion fraction (only 50-65% of low-mass stars appear to have protoplanetary disks, and most transitional and homologously depleted disks are consistent with no accretion) and with the evolutionary features observed in the mid-IR spectra and spectral energy distributions of the disks.

Subject headings: stars: pre-main sequence - stars: formation - protoplanetary disks - stars:late-type

1. Introduction

The Coronet Cluster (also known as CrA) is an obscured star-forming region, located at 170 pc (Knude & Hog 1998), associated to the Herbig Ae star R CrA (Taylor & Storey 1984) and a

---

[1]Max-Planck-Institut für Astronomie, Königstuhl 17, 69117 Heidelberg, Germany

[2]Space Telescope Science Institute, Baltimore, MD 21218, USA

dense molecular core (Loren 1979). Submillimeter, millimeter, IR, and optical surveys (Henning et al. 1994; de Muizon et al. 1980; Wilking et al. 1985; Marraco & Rydgren 1981) found a few HAeBe and T Tauri stars (TTS), suggesting a modest young stellar population of ∼1 Myr in age. X-ray surveys using Einstein, XMM-Newton, ROSAT and Chandra (Walter 1986, 1997; Neuhäuser et al. 2000; Hamaguchi et al. 2005; Garmire & Garmire 2003; Forbrich & Preibisch 2007), less affected by extinction, identified more than 70 sources consistent with young stars, many of which are deeply embedded, all located within a region a bit smaller than 1 pc in diameter. The presence of very embedded sources, including Class 0 objects, suggested a very young region (Henning et al. 1994; Chen et al. 1997; Chini et al. 2003; Groppi et al. 2004,2007; Nisini et al. 2005; Nutter et al. 2005). Optical studies also revealed an important population of low-mass stars, characterized by strong Hα emission (López-Martí et al. 2005). The variety of sources makes the small Coronet cluster a very special place: containing Class 0, I, II, and III objects, it seems to be a relatively quiescent cluster, part of a larger molecular cloud where star formation has occurred only in the densest parts.

Spitzer IRAC/MIPS data and IRS spectra revealed more than 100 low and very low-mass sources, mostly Class I, Class II, and Class III objects, some of them highly extinated, constituting a very young and relatively rich cluster (Sicilia-Aguilar et al. 2008, from now on SA08; Currie & Sicilia-Aguilar 2011). Remarkably, the IRS spectra of the disks around M-type cluster members (which are the bulk of the cluster members) reveal features that are usually accepted as signs of disk evolution: lack of silicate emission, spectral energy distributions (SED) consistent with flattened/settled disks, very low or absent near-IR excesses characteristic of optically thin inner disk/inner holes (SA08). In addition, the estimated disk fraction is lower than expected for a young, embedded cluster, with only 2/3 of the stars being surrounded by protoplanetary disks. Moreover, recent membership searches (López-Martí et al. 2010) have found additional diskless low-mass members, which would reduce the disk fraction to about 50%, a number more consistent with 2-4 Myr old regions than with a 1-2 Myr old cluster (Sicilia-Aguilar et al. 2006; Hernández et al. 2007; Fedele et al. 2010).

Here we present new FLAMES/VLT optical spectroscopy, deep IR imaging with HAWK-I/VLT, and a 870μm map taken with APEX/LABOCA of the Coronet cluster. The data provide spectral types and accretion constrains for most of the remaining low-mass cluster members with moderate extinction, as well as a detailed image of the structures and substructures in the region, with associated Class 0/I embedded sources. The datasets and reduction techniques are discussed in Section 2. Spectral types, accretion, extinction maps, and the cluster structure and embedded members are presented in Section 3. In Section 4 we discuss the age of the Coronet cluster based on the identification of Class 0/I/II/III sources and cluster structure, and finally our conclusions are presented in Section 5.

2. Observations and data reduction

2.1. FLAMES/VLT optical spectroscopy

A large number of members and potential members had been already observed with FLAMES on the UT2/VLT (see SA08). The remaining candidates were done as part of the ESO program 083.C-0079, following a similar scheme to our previous observations. The data were taken in 5 nights (2009 May 24, and 2009 June 3, 17, 18, 19), using FLAMES together with the multifiber spectrograph GIRAFFE and the MEDUSA fibers, which allow to take up to 130 spectra, covering both objects and sky positions. We observed one field centered near the cluster center with three different, intermediate-resolution (R~5600-8600), gratings (L682.2, L773.4, L881.7). The resulting spectra cover thus a large wavelength range from 6440Å to 9400Å, which includes the main accretion features (Hα, Ca II), the Lithium I 6708Å absorption line (indicative of youth), and a large number of photospheric features and absorption bands, required for a spectral type classification of M-type stars. We obtained 3×2700 s exposures with each filter, which ensures good removal of cosmic rays.

The target list included the potential members detected via X-ray (Garmire & Garmire 2003) that had not been observed in our previous run, together with a large number of sky positions (more than 70 in each one of the filters) to ensure a good background subtraction in this region with variable nebular emission. In addition, we also assigned fibers to potential Herbig Haro (HH) objects in the cloud (Wang et al. 2004) and to the objects that, having being detected in our previous FLAMES observations, presented low S/N which made difficult a spectral type classification (especially, the disked stars G-85 and G-87). In total, 12 sources were detected (see Table 1). The lack of detections among the remaining X-ray candidates confirms their status as extragalactic or highly embedded sources, as presumed in SA08 (see Sections 2.2 and 3.3 for more detailed information on individual sources).

The spectra were reduced using standard tasks within IRAF[2]. The data were bias corrected and then extracted with the help of corresponding dome flats, flat fielded, and calibrated in wavelength using the available ThAr lamp. Individual spectra were then combined. No flux calibration was performed, due to the inherent difficulties of calibrating absolute fluxes with a multifiber spectrograph and to the fact that flux calibration is irrelevant for our science case. Since the sky emission is largely variable throughout the field, the sky subtraction was performed in several steps. First, we combined all the sky spectra for each filter and subtracted from all the objects. We then examined each object to determine whether this general sky subtraction properly removed nebular and sky lines. For the objects located in the brightest parts of the nebula (CrA-432, G-80, G-85, G-87, G-88, G-90, G-32, and G-48), for which the standard sky subtraction proved insufficient, we then selected the brightest sky spectra in the region (29 in total) and combined them in a new "bright" sky template, which provided an adequate removal of sky lines. Figure 1 shows the high-

---

[2]IRAF is distributed by the National Optical Astronomy Observatories, which are operated by the Association of Universities for Research in Astronomy, Inc., under cooperative agreement with the National Science Foundation.

and moderate-S/N spectra, and Figures 2 and 3 provide more details on Hα emission and other accretion-related lines.

2.2. HAWK-I

Using the IR camera HAWK-I on the VLT, we observed 11 7.5'×7.5' fields in the Coronet cluster, as part of our ESO program 083.C-0079. The location of the fields was determined by the presence of bright objects, given the minimum magnitude limits of HAWK-I (Ks=8.6 mag, H=9.6 mag, J=9.3 mag). Due to these strong magnitude limitations, the central part of the cluster and most of the areas with strong star formation could not be observed with HAWK-I. Observations took place on 6 different nights, 2009 April 28 and 29, 2009 June 28 and 30, 2009 July 12 and 16, under clear weather and variable seeing conditions (0.5-1.0").

The data was reduced using IRAF tasks within the *ccdred* package for bias correction and flat fielding. For each field and filter, we took 6 dithered images with offsets of 30" and NDIT=20, with total exposure times of 40s (J), 34s (H), and 58s (K). We used the IRAF *daofind* package to identify detections, and *apphot* to perform aperture photometry, with 10 pix aperture and 20-25 pix sky annuli. The photometry was calibrated field-by-field and chip-by-chip as relative photometry by comparing to 2MASS objects present in the fields, using typically 20-120 stars for calibration. Typical calibration errors range from 1 to 5%, depending on the weather conditions. Therefore, signal to noise and background remain the main sources of uncertainty, especially for the fainter objects. The data are complete in a large dynamical range (J=11-18.5 mag, H=11-18.5 mag, K=10.5-18 mag).

Table 2 lists the magnitudes of the previously known sources detected with HAWK-I. Two of the X-ray sources in Garmire & Garmire (2003) that had not been detected with Spitzer nor FLAMES (G-116 and G-119) are now detected with HAWK-I. Their colors suggest that they are most likely extragalactic. Table 2 also includes a comment on the variability of the sources that are also detected in 2MASS. CrA-4107 and CrA-452 show some degree of variability (0.1-0.3 mag, depending on color) which is probably due to rotation and the presence of spots. The J magnitude of G-32 appears more than 1 magnitude fainter in our observations than in the 2MASS catalog, but since the 2MASS magnitude is close to the detection limit of the survey, the HAWK-I data are more accurate.

2.3. APEX/LABOCA 870μm mapping

The 870μm data were obtained with APEX using the LABOCA (Large Apex BOlometer CAmera) bolometer array as part of the ESO program 081.C-0204(A). The data consist of 108 scans in raster map spiral mode, covering an approximate area 30' in diameter. This results in an integration time of 9.2 hours on target. The observations were carried out between 2008 June 21

and 2008 August 24. The opacity was determined with skydips performed at the beginning and the end of the night, varying between τ=0.15-0.44, with a median value 0.2. The flux calibration was estimated observing several sources per night, including Neptune, Uranus, and the secondary calibrators J1957-3845 and J1924-292.

The map was created and calibrated following the pipeline reduction of LABOCA data within the BoA package, especially developed for APEX bolometer data [3]. BoA allows to reduce skydips to derive the opacity, reduce the calibrators, and make the maps. The 108 individual maps were reduced separately, and then coadded to obtain the final map. In each map, the data affected by high acceleration were flagged, as well as the dead and very noisy channels (with rms larger than 5 times the median). Correlated noise was removed by comparing groups of channels. Finally, a linear baseline was fitted and subtracted from the data. The final maps were obtained using the *weakmap* option, which is optimized for weak sources and also provided the best result for the extended emission in the region. The final rms in the map center is $\sim$0.010 Jy, being higher near the brightest sources and the less-integrated edges of the map. The resulting map is displayed in Figure 4.

The second step was to identify and extract the detected structures in the map and to measure the fluxes. The cluster contains a large, dense structure with several peaks as well as some elongated structures and isolated clumps (see Figure 4). The identification and extraction of clumps in the elongated and isolated structures was done using the 2d Clumpfind algorithm, developed by Williams et al. (1994). The 2d Clumpfind works by contouring the data according to user-defined levels in order to determine the presence of structures. To efficiently detect the clumps in the different parts of the map, which have in general different sensitivity, we defined levels according to the local rms. The most noisy parts of the maps were removed before running Clumpfind. The clump identification was repeated 5 times with various sets of levels, and only clumps detected in 3 or more trials are considered to be real. Several sources appear as a single clump or as a collection of adjacent clumps depending on the search parameters. Given the uncertainty on the source boundaries and fluxes, they are listed as a "multiple source" with a unique flux in Table 3, with names that indicate that they are composed of more than one peaks or individual sources (7+10+24, 8+22, 9+14, 13+25, 17+20+26, 18+21). The flux for each clump (or clump collection) was calculated with *clstats2d*, also within the 2d Clumpfind package. The errors in the final flux include the local rms as well as the standard deviation from the flux measured by the slightly different levels imposed for the source detection. The final clumps are listed in Table 3. In general, small, compact structures are detected in a very robust way, while the limits and subdivisions of more extended structures are less well constrained. Several of the submillimeter sources are associated to known IR sources and/or nebular structures (Figure 5).

---

[3]See details in http://www.astro.uni-bonn.de/boawiki/Boa

3. Analysis

3.1. Extinction maps and submillimeter observations

We used the near-infrared colors of the sources detected in the HAWK-I frames to calculate the dust extinction through the CrA cloud. In particular, we adopted the color-excess mapping method nicer (Lombardi & Alves 2001). In the following, we briefly describe the practical implementation of the method. For further details of the method we refer to Lombardi & Alves (2001) and Lada et al. (1994).

The observed colors of stars shining through a dust cloud are related to the dust extinction via the equation:

$$E_{i-j} = (m_i - m_j) - \langle m_i - m_j \rangle_0 = A_j(\frac{\tau_i}{\tau_j} - 1), \tag{1}$$

where E_{i-j} is the color-excess, A_j is extinction, τ_j is optical depth, and $\langle m_i - m_j \rangle_0$ refers to the intrinsic color of stars, measured as the mean color of stars in a field that is free from extinction. We calculated the mean colors using stars in a HAWK-I frame close to $(RA, Dec$ J2000$) = (19$:02:50, -36:46:25$)$, estimated to contain very little extinction based on our earlier, lower-resolution extinction map of the CrA region (Kainulainen et al. 2009). The mean colors in this field were $\langle m_H - m_K \rangle_0 = 0.19 \pm 0.13$ mag and $\langle m_J - m_H \rangle_0 = 0.47 \pm 0.15$ mag. For the ratios of optical depths we adopted $\tau_H/\tau_K = 1.67$, $\tau_J/\tau_H = 1.48$, and $\tau_V/\tau_K = 8.77$ (Cardelli et al. 1989). Before calculating the extinction, we removed from the HAWK-I detections the previously known members of the CrA cloud, based on the identifications given by SA08, Forbrich & Preibisch (2007), and López-Martí et al. (2005, 2010).

Observations in three broadband filters (JHK_S) result in measurements of two color excesses, namely E_{H-K} and E_{J-H}, towards each source. These two measurements were combined to yield extinction values towards the sources following the formalism presented in Lombardi & Alves (2001). The derived extinction values were then used to produce a regularly sampled map by computing the mean extinction in regular intervals (map pixels) of $24''$, using a Gaussian with $FWHM = 48''$ as a spatial weighting function. In this resolution, the maximum extinction in the resulting map reaches $A_V \approx 50$ mag, with $A_V \approx 20$ mag corresponding to 1-2 stars per pixel. The error in the map depends on extinction, with 3-σ being about 0.8 mag at $A_V = 0$ mag and 7 mag at $A_V = 50$ mag.

Figure 6 shows the resulting extinction map, combined with the 2MASS extinction map in the regions not included in our HAWK-I imaging. There is an excellent agreement between the 870μm clumps and the regions of high extinction. Nevertheless, the extinction map reveals large parts of the molecular cloud that are not detected in the LABOCA survey due to their lower column density. The most massive stars in the region are associated to the zones with the highest extinction and strongest submillimeter emission, as expected. The distribution of low mass members with respect to the cloud is less clear, also due to the fact that the non-biased survey for low-mass members was done only in the central part of the cluster.

3.2. Spectral types, extinction, and accretion

The FLAMES spectra allow to determine spectral types for the objects with good S/N. We followed a similar scheme as used in SA08, using the spectral indices and bands from Martín et al. (1996), called PC1, PC2, PC3 and PC4, and the R1, R2, R3, TiO 8465 indices in Riddick et al. (2007). The additional indices VO 2 and VO 7445 from Riddick et al. (2007) were also used to refine the spectral types for objects M5 or later. Table 4 offers a list of the relevant indices and their valid spectral type ranges. A combination of spectral types and the available JHK photometry allows to estimate the extinction of the objects (see below). For the objects with intermediate to high extinction (A_V >3 mag), we gave priority to the results derived from the indices PC1, PC2, R1, R2, R3, TiO 8475, VO 2, and VO 7445, which are derived from flux rations in adjacent parts of the spectrum, being thus less sensitive to extinction. For objects like CrA-432, that have nearly no signal in the bluer part of the spectrum (L682.2), we used only the indices involving the longer-wavelength parts. For every object, the spectral types derived from each index were compared, and those that largely deviated from the typical value were removed and not used (deviating indices are usually affected by noise, atmospheric features, and/or poor S/N in one of the bands). In general, between 2-6 indices were used for the classification of each star, depending on the spectral type, extinction, and S/N in the three spectral bands. The errors in the spectral types are calculated as the standard deviation of the values derived from each valid index. The classification scheme failed for the object G-1, which appears earlier than the rest. It was thus classified by comparison to solar-type T Tauri star templates obtained from a combination of Hectospec/MMT observations in the Cep OB2 region (Sicilia-Aguilar et al. 2005).

Two of the objects, G-85 and G-87, are highly extincted (A_V >14 mag). After a first tentative classification, we used the preliminary A_V value to de-redden the spectra (using IRAF task *deredden* within the *onedspect* package) before the final classification. Examination of two objects revealed that their spectral types are earlier than M2, a range for which the mentioned indices are not valid. We thus derived their spectral types using our solar-type T Tauri templates as we did for G-1 (see Figure 7). Note that G-85 and G-87 had been previously observed in SA08, but the new improved S/N (due to better weather and seeing conditions) now allows to refine their spectral types, confirming them to be earlier than previously thought by about 2-3 subtypes (having G-85 and G-87 spectral types M0.5±1.5 and M1.5±1.5, respectively). The star CrA-468, also known as G-49, had also previously been observed with FLAMES (SA08). The new spectrum is fully consistent with the previous one (see Figure 2), resulting in a similar Hα classification and spectral type (M4.0±1.0 versus M3.5±0.5). The final spectral types are listed in Table 1.

The individual extinction values were derived from the JHK 2MASS photometry, comparing to standard colors for stars and BD (Bessell et al. 1998; Kirkpatrick et al. 1995). The extinction was derived from E(J-H) and E(H-K), using the relations in Cardelli et al. (1989), A_V=10.87 E(J-H) and A_V=5.95 E(J-K) mag, valid for a standard galactic extinction law. For most sources, the agreement between A_V obtained from the two different colors suggests that most of the extinction is due to foreground and cloud material, with no evidence of anomalous extinction that could be

caused by processed grains in the circumstellar environment, despite the presence of strong disk emission in some of the objects. Only in the cases of CrA-4108 and CrA-468 we found large differences between the extinction values derived from different colors, which could indicate the presence of anomalous extinction/scattering. In the case of CrA-468, the Spitzer data reveals it is located near substantial nebular material. CrA-4108 is out of our Spitzer field.

The presence or lack of accretion was established by measuring the equivalent width and examining the profile and line width at 10% of the peak for the Hα line (see Figure 2). The lines were measured using IRAF tasks within the *splot* tool. We adopted the classification of White & Basri (2003) for the limiting EW of accreting and non-accreting stars, depending on their spectral type. Given that the line width is a more powerful tool than the EW to detect weak accretors (Sicilia-Aguilar et al. 2006), we consider an object to be accreting if its 10% line width exceeds 200 km/s (Natta et al. 2005). In some cases, like G-1, the broad profile is evident, although the EW is much smaller than the canonical limit for accretion in an M0.5 object, so we list it as an accretor. The presence of accretion was also checked in other lines, like the Ca II IR triplet and the 6678Å He I line. The lack of Ca II emission in G-1 suggests an accretion rate below 10^{-9} M$_\odot$/yr (Muzerolle et al. 1998). All the spectral lines measured are listed in Table 1.

The new accretion determination, together with our previous measurements in SA08, confirms that most of the low-mass Coronet members have very low accretion rates, with CrA-432 and G-85 being the only exceptions. As we found in SA08, transitional and highly evolved disks (like G-87) do not show evidence of ongoing accretion (within the 10^{-10}-10^{-11} M$_\odot$/yr limit imposed by the FLAMES spectral resolution). This differs from the observations of solar-type stars, for which usually half or more of the transition disks are found to be accreting (Sicilia-Aguilar et al. 2006, 2010; Muzerolle et al. 2010; Fang et al. 2009). All objects without IR excesses are consistent with no accretion. For the objects out of the Spitzer fields (CrA-4108 and CrA-452), the spectroscopy reveals no evidence of accretion. CrA-4108 shows marginal emission that could belong to He I at 5875Å, but the lack of Ca II lines in emission suggests that the object is not accreting (see Figure 3). The Herbig Haro (HH) object G-80 was reobserved in this program, confirming again its shock nature via [N II], [S II], and asymmetric Hα profile. Finally, three sources that were not detected with Spitzer (G-48, G-88, and G-90) are now marginally detected, with G-88 and G-90 displaying broad Hα emission that suggests they are very embedded Class I sources. Their condition as embedded sources is also consistent with their location within one of the strongest submillimeter structures.

3.3. Massive disks, protostars, and prestellar condensations

As listed in Table 3, several of the detected 870μm sources are related to known Class II and embedded sources in the region. Assuming a distance of 170 pc, the 18.6" beam results in a ~3000 AU size. Condensations #2, 3, 4, 5, and 27 are associated to the previously known sources IRS 2, IRAS 18595-3712, VV CrA, HD 176386b, and S CrA, respectively. In addition, #3 and 4 also

correspond to the millimeter emitting objects 23 and 24 from Chini et al. (2003). We combined the pre-existing data from Spitzer (see Currie and Sicilia-Aguilar 2011 for the data on IRS 2, S CrA, and HD 176386b and the reduction procedures applied to the rest of the sources), AKARI (Kataza et al. 2010), and millimeter/submillimeter data (Gezari et al. 1999; Chini et al. 2003; Nutter et al. 2005), to trace the SEDs of these objects. Table 5 summarizes the available data for the SEDs shown in Figure 8.

The 870 μm flux from IRS 2 is in good agreement with previous submillimeter measurements of the source, and consistent with an embedded Class I source. For S CrA, our data is also in very good agreement with previous submillimeter observations, and its SED is consistent with a massive protoplanetary disk. Both IRS 2 and S CrA appear as marginally spatially extended, which suggests the presence of envelopes or surrounding cloud material. In both cases, the estimated size of the envelopes would be of the order of $\sim$5000 AU (assuming a distance of 170 pc; Knude & Hog 1997). The emission associated to HD 176366b is extended, and appears related to the warm cloud material detected in the Spitzer images.

To the south of the CrA region, two condensations, associated to the sources VV CrA and IRAS 18595-3712, are detected. The emission associated to the binary VV CrA is very compact and probably corresponds to the protoplanetary disk of the main source plus that of the disk and envelope of the embedded companion (Ratzka et al. 2008). The submillimeter emission around IRAS 18598-3712 appears slightly extended to the East, suggesting the presence of a larger envelope. The emission at longer wavelengths for this source is indeed consistent with a black body of T=70 K (see Figure 8). The extinction map reveals substantial cloud material in this direction, which could also produce the extended emission near the source. The SED of this object suggests the presence of a large amount of material, which could include the source envelope plus contamination from the surrounding cloud.

Regarding the rest of clumps detected in the LABOCA maps, they correspond to more complex regions that include several embedded sources and to denser nebular material in the region, which is confirmed by the extinction maps. This is the case of clump #1, which includes the sources T CrA, R CrA, V710, and IRS 7e/w,among others (see Figure 5 right). The peak of the emission appears to the South-West of IRS 7, which is consistent with the observations of Chini et al.(2003) and Nutter et al. (2005). The embedded X-ray source G-17 is associated to clump #12. Although the size of the clump is too large for it to be considered as the same and single object, the presence of this X-ray source near the emission peak of clump #12 indicates that G-17 is most likely a very embedded low-mass protostar, as it had been suggested by SA08. The star CrA-465 appears superimposed to the clump #9, but the submillimeter emission is most likely due to background cloud material not related to the source, given both the size of the structure and the low extinction of CrA-465 (A_V=0.08±0.04; SA08).

The strongest emission in the LABOCA map is thus associated to the largest concentration of intermediate-mass members, as it would be expected. The most massive stars appear thus along

the two arms (running in the HD 176386 to VV CrA direction, and in the HD 176386 to S CrA directions, respectively) of the molecular cloud, clearly depicted in the extinction maps (Figure 6). It is not possible to establish a further correlation between the rest of structures with submillimeter emission and the distribution of cluster members in the region, since so far only the most central part of the cluster has been explored for membership in a systematic way.

4. The age of the Coronet cluster and the star forming region

The age of the Coronet cluster has been subject to intense debate. While most observations suggested an age of 1-3 Myr (Meyer & Wilking 2009), the presence of a Class 0 source and several embedded objects was rather consistent with a younger cluster, ∼0.5-1 Myr (Henning et al. 1994; Chen et al. 1997; Chini et al. 2003; Nisini et al. 2005; Nutter et al. 2005; Groppi et al. 2004, 2007). Nevertheless, both the disk frequency (∼50-65%) and the disk characteristics among the low-mass, M-type population appear closer to the values observed in older regions than to a 1 Myr-old cluster (SA08; López-Martí et al. 2010; Currie & Sicilia-Aguilar 2011). On the other hand, the presence of substantial amounts of nebular material would be inconsistent with an age beyond 3 Myr (Hartmann et al. 2001; Ballesteros-Paredes & Hartmann 2007). Finally, spectroscopic data also reveal a low accretion fraction, with all the transition and settled/dust depleted disks showing no evidence for accretion, which has been typically related to few-Myr old regions (Muzerolle et al. 2010).

Few-Myr age differences between cluster members are common in many regions, and many clusters include sequential star formation, which results in the presence of more than one star-forming event and thus two or more populations with different ages (e.g. Sicilia-Aguilar et al. 2005, 2006). Nevertheless, the Coronet cluster is special because of it compactness: the members studied here are located within the densest region of the CrA nebula, which is less than 1.3 pc across (adopting a distance of 170 pc; Knude & Hog 1997). A strong correlation between the size of the region and the age dispersion of the cluster members has been observed in our galaxy and in the Magellanic Clouds (Elmegreen 2000): the age dispersion of cluster members is of the order of the crossing time in the region, which for the Coronet cluster is smaller than 2 Myr. In fact, regions similar to the Coronet cluster in size and stellar content (e.g. the η Cha cluster) are usually found to be strongly coeval (Lawson et al. 2009).

We have thus estimated the age of the cluster by placing the known members in a color-magnitude diagram. A color-magnitude diagram is preferred to a HR diagram since it involves less transformations of the original data that result in increased uncertainties. The effect of the data uncertainties is also easier to control and determine in a color-magnitude diagram, since it does not involve propagation of non-independent errors. Our knowledge of spectral types allows to correct individually for the extinction, which is particularly important in regions with non-uniform cloud material. Figure 9 displays the near-IR color-magnitude diagram H vs. J-H of the low-mass T Tauri members of the Coronet cluster, using their 2MASS and HAWK-I data, together with the

isochrones from Baraffe et al. (1998) for the distances of 130 (only the 1 and 2 Myr isochrones) and 170 pc (1, 2, 5, and 10 Myr isochrones). These two distances correspond to the estimates given by Marraco & Rydgren (1981, 130 pc) and the more recent one by Knude & Hog (1998, 170 pc). Given that age and distance are degenerated, we consider both extreme values in order to ascertain the potential errors in the age determination. Table 6 summarizes the data of the sources used in the HR diagram. The extinction of the objects has been corrected using their individual values in Figure 9. In addition to the photometric errors, we also display the uncertainties in the extinction, which are related to the uncertainties in the spectral types of the objects. Due to the fact that there is little spread for the lower-mass objects in the J-H direction at these ages, it is hard to determine an age for the cluster from these objects. Nevertheless, the location of the isochrone "kink" for the early M-type stars is more consistent with a distance of 170 pc. In any case, for either a distance of 130 or 170 pc, and considering the limitations imposed by the small number of objects with early M-type in the cluster, the distribution in the color-magnitude diagram of the early M-type objects suggests that the population has an age in the range 0.5-2 Myr. For the most plausible distance of 170 pc, the age would be in the 0.5-1 Myr range. This is in agreement with the conclusions of Chen et al. (1997), based on the bolometric temperature and luminosity of young stellar objects (YSO), which stated that the CrA region is younger than 2 Myr and most likely, younger than Taurus, even assuming a distance of 130 pc.

This age estimate is also consistent with the presence of Class 0 and very embedded Class I sources in the region. Nevertheless, the relatively low disk fraction found among T Tauri stars (2/3 or lower; SA08, López-Martí et al. 2010) is atypical for such a young region. The "evolved" features of the disks (lack of silicate emission as expected from disks with large grains, presence of disks with inner holes and small dust-depleted disks, SEDs consistent with strong dust settling; SA08, Currie & Sicilia-Aguilar 2011) are hard to understand for a 1 Myr-old cluster. Some of the objects (CrA-205, CrA-4108, CrA-4109) are located at larger distances from the center of the cloud, and may have thus a larger age difference with the main cluster. Nevertheless, the lack of spectral types and extinction (for CrA-205 and CrA-4109) and the position of the source itself in a place where the isochrones are degenerated (for CrA-4108) do not let us test this hypothesis. Although the Coronet is younger than (or has a similar age to) Taurus, its median disk SED for M-type stars is well below the Taurus median SED for the same type of objects (SA08). This may trace back to the formation history of the region and/or the evolution of disks around these low-mass objects in relatively quiescent and sparse regions. It could also be explained if the cluster were unusually compact (and actually not sparse) and interactions would affect the disk structure and evolution. Further observations in a more extended area would be required to check for the presence of other populations.

5. Conclusions

We present new multiwavelength data for the Coronet cluster, including optical spectroscopy obtained with the FLAMES multifiber spectrograph, $870\mu m$ mapping obtained with the LABOCA bolometer on the APEX telescope, and near-IR imaging from HAWK-I. The optical data allows to derive spectral types, individual extinctions, and accretion status for the remaining X-ray members, completing the work started by SA08. The submillimeter data reveals the densest structures of the cloud, as well as the circumstellar disks and envelopes of some intermediate-mass and T Tauri members. The near-IR imaging provides photometry for some of the faintest members and allows to derive extinction maps, which trace the cloud material in low-density regions that are not detected in the submillimeter. Both extinction and submillimeter maps reveal a large cloud where star formation has only occurred along two arms that contain the densest parts of the molecular cloud, resulting in a quite compact cluster.

By placing the extinction-corrected photometry of the known low-mass members in a near-IR color-magnitude diagram and comparing with the Baraffe et al. (1998) isochrones, we estimate the age of the cluster to be below 2 Myr, and probably within the 0.5-1 Myr range. This agrees with previous studies (suggesting an age <3 Myr; Meyer & Wilking 2009) as well as with the presence of substantial cloud material and highly embedded Class I and Class 0 objects, and it is also in agreement with the compactness of the region where most members are located. But a young age is in a strong contrast with the relatively low disk fraction ($\sim$65-50%; SA08; López-Martí et al. 2010) and the evidence of disk evolution (inner holes, lack of silicate features, strong settling, and dust depleted disks; SA08; Currie & Sicilia-Aguilar 2011) observed among the lower-mass and M-type cluster members. Further observations will be required to examine the presence of other low-mass members in the region and determine whether the region contains more than one population.

REFERENCES

Ballesteros-Paredes, J., Hartmann, L., 2007, Rev. Mex. A.A., 43, 123

Baraffe, I.,Chabrier, G., Allard, F., & Hauschild, P., 1998, AA, 337, 403

Bessell, M. S.; Castelli, F.; Plez, B., 1998, A&A, 333, 231

Cardelli, J. A., Clayton, G. C., & Mathis, J. S. 1989, ApJ, 345, 245

Chen, H.; Grenfell, T. G.; Myers, P. C.; Hughes, J. D., 1997, ApJ, 478, 295

Chini, R. et al. 2003, A&A, 409, 235

Currie, Th., & Sicilia-Aguilar, A., 2011, ApJ in press

De Muizon, M., Rouan, D., Lena, P., Nicollier, C., Wijnbergen, J., 1980, AA, 83, 140

Elmegreen, B. G. 2000, ApJ, 530, 277

Fang, M., van Boekel, R., Wang, W., Carmona, A., Sicilia-Aguilar, A., & Henning, T. 2009, A&A, 504, 461

Fedele, D., van den Ancker, M. E., Henning, T., Jayawardhana, R., & Oliveira, J. M. 2010, A&A, 510, A72

Forbrich, J.; Preibisch, T., 2007, A&A 475, 959

Garmire, G., & Garmire, A., 2003, Astron. Nachr. 324, 153

Gezari, D. Y., Pitts, P. S., & Schmitz, M. 1999, VizieR Online Data Catalog, 2225, 0

Groppi et al., 2004, ApJ, 612, 946;

Groppi, C. E., Hunter, T. R., Blundell, R., & Sandell, G. 2007, ApJ, 670, 489

Hamaguchi, K., et al. 2005, ApJ 618, 360

Hartmann, L., Ballesteros-Paredes, J., Bergin, E., 2001, ApJ 562, 852

Henning, Th.; Launhardt, R.; Steinacker, J.; Thamm, E., 1994, A&A, 338, 223

Hernández, J., Hartmann, L., Megeath, S.T.,et al., 2007, ApJ, 662, 1067

Kainulainen, J., Beuther, H., Henning, T., & Plume, R. 2009, A&A, 508, L35

Kataza, H., Alfageme, C., Cassatella, A., Cox, N., Fujiwara, H., Ishihara, D., Oyabu, S., Salama, A., Takita, S., and Yamamura, I., 2010, AKARI-IRC Point Source Catalogue Release note Version 1.0

Kirkpatrick, J. D.; Henry, T. J.; Simons, D. A. 1995, AJ, 109, 797

Knude, J.; Hog, E. 1998, A&A 338, 897

Lada, C. J., Lada, E. A., Clemens, D. P., & Bally, J. 1994, ApJ, 429, 694

Lawson, W. A.,Lyo, A.-R., Bessell, M.S., 2009, MNRAS, 400, L29

Lombardi, M., & Alves, J. 2001, A&A, 377, 1023

López-Martí, B., Eislöffel, J., Mundt, R., 2005, AA, 444, 175

López Martí, B., et al. 2010, A&A, 515, A31

Loren, R. B., 1979, ApJ, 227, 832

Marraco & Rydgren 1981, AJ, 86, 62

Martín, E., Rebolo, R., Zapatero-Osorio, M.R., 1996, ApJ, 469, 706

Meyer, M. R., & Wilking, B. A. 2009, PASP, 121, 350

Muzerolle, J., Hartmann, L., Calvet, N., 1998, AJ 116, 455

Muzerolle, J., Allen, L. E., Megeath, S. T., Hernández, J., & Gutermuth, R. A. 2010, ApJ, 708, 1107

Natta, A., Testi, L., Randich, S., Muzerolle, J., 2005, Mem. S.A.It., 76, 343

Neuhäuser, R., et al., 2000, A&A, 146, 323

Nisini, B.; Antoniucci, S.; Giannini, T.; Lorenzetti, D., 2005, A&A, 429, 543

Nutter, D. J., Ward-Thompson, D., & André, P. 2005, MNRAS, 357, 975

Ratzka, T., Leinert, C., Przygodda, F., & Wolf, S. 2008, The Power of Optical/IR Interferometry: Recent Scientific Results and 2nd Generation, 519

Riddick, F. C.; Roche, P. F.; Lucas, P. W., 2007, MNRAS, 381, 1067

Sicilia-Aguilar, A.; Hartmann, L.; Hernández, J.; Briceño, C.; Calvet, N., 2005, AJ, 130, 188

Sicilia-Aguilar, A., et al., 2006,ApJ 638, 897

Sicilia-Aguilar, A.; Henning, Th.; Juhász, A.; Bouwman, J.; Garmire, G.; Garmire, A., 2008, ApJ, 687, 1145

Taylor & Storey, 1984, MNRAS, 209, 5

Walter, F., 1986, ApJ, 306, 573

Walter, F., et al., 1997, AJ, 114, 1544.

Wang, H., Mundt, R., Henning, Th., Apai, D., 2004, ApJ 617, 1191

White, R., & Basri, G., 2003, ApJ, 582, 1109

Wilking et al., 1985, ApJ, 293, 165

Williams, J., et al. 1994, ApJ 428, 693

Table 1.   Spectral types, extinction, and main lines

Name	ID/Coord.	Spec. Type	A_V (mag)	Hα	Li I	[N II]	[S II]	He I	Ca II	K I	Na I^R	Na I^I	Comments
CrA-4108	19020968-3646345	M3.5 (±1.0)	1.2±1.1	-7.6	0.52	—	—	-0.2	0.31/0.85:/0.54	2.07/1.39	1.16/1.47	1.12/1.49	NA
CrA-432	19005974-3647109	M4.0 (±1.0)	2.7±0.2	-46	—	—	—	-2.8:	-0.34/-0.59/-0.25	2.43/1.89	1.12/1.50	1.18/1.53	A
CrA-452	19004455-3702108	M2.5 (±0.5)	1.7±0.2	-2.6	0.51	—	—	—	0.23:/0.83:/0.80	1.45/0.82	0.83/1.15	0.78/1.03	NA
CrA-468*	19014936-3700285	M3.5 (±0.5)	0.6±0.7	-2.8	0.53	—	—	—	0.5/0.7/0.7	1.77/1.07	0.99/1.28	1.02/1.26	NA
G-1	19022708-3658132	M0.5 (±0.5)	3.4±0.2	-3.8	0.58	—	—	—	0.4/1.5/1.1	1.28/0.62	0.62/0.77	0.59/0.79	A
G-32	19015833-3700267	—	—	-4:	—	—	—	—	—	—	—	—	NA
G-48	19:01:49.8 -36:52:43	—	—	-9:	—	—	—	—	—	—	—	—	Uncertain
G-80	19:01:35.7 -37:02:32	—	—	-275:	—	-25/-83	-170:/-41:	—	—	—	—	—	HH
G-85	19013385-3657448	M0.5 (±1.5)	19±2	-31	—	—	—	—	-2.6/-2.8/-2.1	2.27/1.06	0.72/0.98	0.76/0.98	A
G-87	19013232-3658030	M1.5 (±1.5)	16±2	-3:	—	—	—	—	0.15/0.52/0.91	2.16/2.79	0.51/0.89	—/1.56	NA:
G-88	19:01:32.2 -36:51:20	—	—	-13	—	—	—	—	—	—	—	—	A:
G-90	19:01:31.4 -36:52:53	—	—	-7.4	—	—	—	—	—	—	—	—	A:

Note. — ines observed in the FLAMES spectra. Uncertain values are marked by ":". The field "ID/Coord." provides the 2MASS IDs of the objects, or their coordinates in case they were not detected by 2MASS. The EW are given in Å, with negative values used for emission lines. The wavelengths of the listed lines are 6562Å (Hα), 6708Å (Li I), 6548/6584Å ([N II]), 6717/6731Å ([S II]), 6678Å (He I),8498/8542/8662Å (Ca II IR triplet), 7665/7699Å (K I), 8183/8185Å (Na I). For the Na I lines, we give two values measured in the L773 and L881 spectra ('R' for red, 'I' for IR), respectively. The comments list the presence of accretion (A) or no evidence for accretion (NA), Herbig-Haro objects (HH). The accretion classification is made taking into account the Hα EW, Hα profile, and presence of the Ca II in emission. * The object CrA-468 is also known as G-49 (SA08).

Table 2.   HAWK-I data for known Coronet members and potential members

Name	RA (J2000)	DEC (J2000)	RA (deg)	DEC (deg)	J (mag)	H (mag)	K (mag)	Comments
CrA-4107	19:02:54.64	-36:46:19.1	285.727661	-36.771973	12.577±0.009	12.008±0.015	11.631±0.015	variable (0.1-0.2 mag)
CrA-452	19:00:44.55	-37:02:10.8	285.185638	-37.036343	11.853±0.018	—	—	variable (∼0.3 mag)
CrA-465	19:01:53.74	-37:00:33.9	285.473907	-37.009418	14.078±0.079	13.479±0.061	13.001±0.070	
CrA-468	19:01:49.36	-37:00:28.5	285.455658	-37.007915	12.508±0.079	12.037±0.061	—	also called G-49
G-14	19:02:12.01	-37:03:09.3	285.550049	-37.052582	13.453±0.052	12.633±0.029	12.200±0.027	
G-30	19:02:00.12	-37:02:22.0	285.500488	-37.039444	12.064±0.079	—	—	
G-32	19:01:58.33	-37:00:26.7	285.493042	-37.007416	18.134±0.080	15.418±0.061	13.650±0.070	
G-116	19:01:15.40	-36:52:36.0	285.314178	-36.876667	21.116±0.167	18.962±0.115	18.493±0.068	prob. extragal.
G-119	19:01:07.90	-36:51:21.0	285.282928	-36.855831	19.252±0.039	18.347±0.038	17.831±0.040	prob. extragal.

Note. — HAWK-I JHK magnitudes for the detected known Coronet members and potential members (based on Spitzer and X-ray data). G-116 and G-119 are probably extragalactic sources.

Table 3.   Clumps and structures found in the LABOCA map

Name	RA (J2000)	DEC (J2000)	Extension (beam)	Integrated Flux (Jy)	Related sources
1	19:01:53.9	-36:58:03	96±8	33.3±0.8	COA2, Ch10,11,12, see Fig. 5
2	19:01:42.5	-36:58:39	6±1	1.44±0.02	IRS2,Ch9
3	19:02:59.4	-37:07:45	22±7	3.40±0.35	Ch23, IRAS 18595-3712
4	19:03:07.9	-37:13:04	10±2	1.65±0.07	Ch24, VV CrA
5	19:01:39.5	-36:53:29	35±7	4.55±0.43	HD-176386B,Ch6,7,8
6	19:02:18.3	-37:01:41	27±20	2.1±1.1	Ch21
7+10+24	19:03:06.4	-37:14:53	32±5	2.40±0.15	COA4
8+22	19:00:55.4	-36:55:27	29±7	1.95±0.28	
9+14	19:01:57.0	-37:01:05	20±5	1.43±0.18	Ch14
11	19:02:11.4	-36:56:22	15±7	1.08±0.33	G-17
12	19:02:13.7	-36:57:26	7±1	0.45±0.05	Ch19
13+25	19:02:11.4	-37:00:47	16±2	1.15±0.08	Ch18:
16	19:02:24.3	-36:56:50	13±4	0.73±0.15	
17+20+26	19:01:05.3	-36:54:14	35±13	1.88±0.53	Ch2,3,4
18+21	19:01:13.7	-36:54:23	27±6	1.33±0.03	Ch5
19	19:02:33.5	-37:02:08	13±6	0.63±0.03	
23	19:02:18.3	-37:04:43	13±5	0.48±0.15	
27	19:01:09.1	-36:57:26	6±2	0.77±0.02	S-CrA,Ch1

Note. — Clumps detected with 2d Clumpfind in the 870μm map. When the identification of a structure as one or several clumps depends on the parameters used by 2d Clumpfind, we list it as a "multiple structure" (e.g. 7+10+24). The last column indicates whether the clump is associated to known sources or structures detected at different wavelengths. Millimeter clumps from Chini et al. (2003) are marked as Ch#. CO detections from Vilas-Boas et al. (2000) are marked as COA#. Uncertain values are marked with ":". Note that the association to a source is merely the coincidence of coordinates, it does not mean that the submillimeter clump and the (optical, X-ray, CO) source are the same object (see text for details).

Table 4.   Spectral typing indices

Name	λ Numerator	λ Denominator	Range	Calibration	Reference
PC1	7030-7050	7525-7550	M3-M9	-0.06+2.95 X	1,2
PC2	7540-7580	7030-7050	M4-M8	-0.63+3.89 X	1,2
PC3	8235-8265	7540-7580	M3-M9	-8.01+14.08 X-2.81 X^2	2
PC4	9190-9225	7540-7580	M3-M9	-0.94+4.66 X-0.52 X^2	2
R1	8025-8130	8015-8025	M2.5-M8	$2.8078+21.085(X-1.044)-53.025(X-1.044)^2+60.755(X-1.044)^3$	3
R2	8415-8460	8460-8470	M3-M8	$2.9091+10.503(X-1.035)-14.105(X-1.035)^2+8.5121(X-1.035)^3$	3
R3	(8025-8130)+(8415-8460)	(8015-8025)+(8460-8470)	M2.5-M8	$2.8379+19.708(X-1.035)-47.679(X-1.035)^2+52.531(X-1.035)^3$	3
TiO 8465	8405-8425	8455-8475	M3-M8	$3.2147+8.7311(X-1.085)-10.142(X-1.085)^2+5.6765(X-1.085)^3$	3
VO 2	7920-7960	8130-8150	M3-M8	$2.6102-7.9389(X-0.963)-8.3231(X-0.963)^2-14.660(X-0.963)^3$	3
VO 7445	0.5625(7350-7400)+0.4375(7510-7560)	7420-7470	M5-M8	$5.0881+17.121(X-0.982)+13.078(X-0.982)^2$	3

Note. — Indices used for spectral typing. The wavelengths are given in Å. In the calibration, X represents the index, and the resulting number indicates the M subtype. References: 1= Kirkpatrick et al. (1996); 2= Martín et al. (1996); 3= Riddick et al. (2007). The lineal relations for PC1 and PC2 are obtained by fitting together the objects in references 1 and 2.

Table 5.　Fluxes for the individual sources detected with LABOCA

Wavelength (μm)/Filter	IRS2	IRAS 18595-3712	VV CrA	HD 176386	S CrA	References
0.44/B	—	—	—	4.67	0.0335	SIMBAD
0.55/V	—	—	—	4.38	0.0656	SIMBAD
1.22/J	0.0050±0.0001	0.00007:	0.179±0.005	1.43±0.10	0.828±0.019	2MASS
1.63/H	0.129±0.004	0.0005	0.729±0.030	1.03±0.10	1.54±0.04	2MASS
2.19/K$_s$	0.949±0.023	0.0010±0.0001	2.028±0.040	0.89±0.08	2.29±0.05	2MASS
3.6	—	0.00976±0.00004	4.753±0.017	0.2059±0.0004	2.66±0.01	IRAC/Spitzer
4.5	—	0.0224±0.0004	6.160±0.022	0.1388±0.0004	3.16±0.01	IRAC/Spitzer
5.8	—	0.0224±0.0010	15.21±0.05	[a]	3.81±0.02	IRAC/Spitzer
8.0	7.71±0.02	0.0138±0.0004	—	[a]	4.17±0.02	IRAC/Spitzer
9.0	—	—	24.12±0.23	—	4.41±0.08	AKARI
12	13:	—	31.9:	—	—	IRAS
18	—	0.884±0.026	39.7±4.3	—	7.19±0.10	AKARI
23.9	—	2.474±0.001	—	—	—	
25	50:	3.69:	69.1:	—	—	IRAS
60	—	38.9:	131:	—	—	IRAS
65	—	—	—	—	13.8±4.3	AKARI
100	—	—	95.2:	—	—	IRAS
450	12±1	—	—	—	3±0.3	Nutter et al.(2005)
850	2.0±0.7	—	—	—	0.7±0.2	Nutter et al.(2005)
870	1.44±0.02	3.40±0.35	1.65±0.07	4.55±0.43[b]	0.77±0.02	This work
870	—	—	—	—	0.507±0.260	Gezari et al. (1999)
1200	1.32±0.70	0.672±0.340	—	—	0.29±0.15	Chini et al. (2003)

Note. — Multiwavelength fluxes for the sources in Figure 8. All the fluxes are in Jy. The data include 2MASS JHK photometry and Spitzer data (Skrutskie et al. 2006; Currie & Sicilia-Aguilar 2010), IRAS observations (Wilking et al. 1992), AKARI data (9, 18, and 65μm; Kataza et al. 2010), and mm/submm points (Gezari et al. 1999; Chini et al. 2003; Nutter et al. 2005). The Spitzer data for VV CrA and IRAS 18595-3712 has not been published previously, but it was obtained as aperture photometry with MOPEX on the BCD mosaics using the same techniques and parameters exposed in Currie & Sicilia-Aguilar (2010). Uncertain values are marked by ":". [a] Extended emission, the source cannot be extracted. [b] The emission is very extended and probably includes part of the molecular cloud, in addition to the source.

Table 6.   Summary of JHK data for sources in the HR diagram

Name	ID	J (mag)	H (mag)	K (mag)	Sp. Type	A_V (mag)
CrA-4108	19020968-3646345	12.580±0.023	11.972±0.023	11.634±0.019	M3.5	1.2± 1.1
CrA-4110	19011629-3656282	12.954±0.021	12.314±0.021	11.897±0.021	M5	1.3± 0.4
CrA-4111	19012083-3703027	13.233±0.024	12.687±0.023	12.402±0.024	M4.5	0.1± 0.5
CrA-432	19005974-3647109	14.190±0.026	13.333±0.035	12.821±0.030	M4.0	2.7± 0.2
CrA-452	19004455-3702108	11.571±0.024	10.766±0.025	10.447±0.023	M2.5	1.7± 0.2
CrA-453	19010460-3701292	13.338±0.024	12.524±0.025	12.075±0.023	M4.5	0.4± 0.3
CrA-465	19015374-3700339	14.084±0.026	13.401±0.033	13.015±0.033	M7.5	0.2± 1.0
CrA-466	19011893-3658282	12.834±0.024	11.245±0.025	10.453±0.021	M2.0	8.1± 0.4
CrA-468	19014936-3700285	12.498±0.026	11.891±0.025	11.603±0.024	M3.5	0.6± 0.7
G-1	19022708-3658132	9.307±0.024	8.292±0.038	7.900±0.016	M0.5	3.4± 0.2
G-14	19021201-3703093	13.408±0.029	12.582±0.029	12.145±0.021	M4.5	1.9± 0.1
G-30	19020012-3702220	11.859±0.026	11.238±0.024	11.003±0.026	M3.5	0.1± 0.5
G-65	19014041-3651422	13.898±0.032	11.629±0.023	10.481±0.019	M1.5	13.8± 0.5
G-85	19013385-3657448	14.448±0.030	11.910±0.023	10.474±0.019	M0.5	19± 2
G-87	19013232-3658030	14.853±0.037	12.622±0.029	11.432±0.023	M1.5	16± 2
G-94	19012901-3701484	11.637±0.024	10.956±0.023	10.663±0.021	M3.5	0.6± 0.1
G-95	19012872-3659317	10.828±0.023	9.591±0.025	9.002±0.019	M1.0	5.0±0.4
G-102	19012562-3704535	12.363±0.023	11.654±0.021	11.299±0.023	M5.0	0.7± 0.1

Note. — Compilation of 2MASS magnitudes, spectral types, and extinctions of the members with known spectral types used in Figure 9.
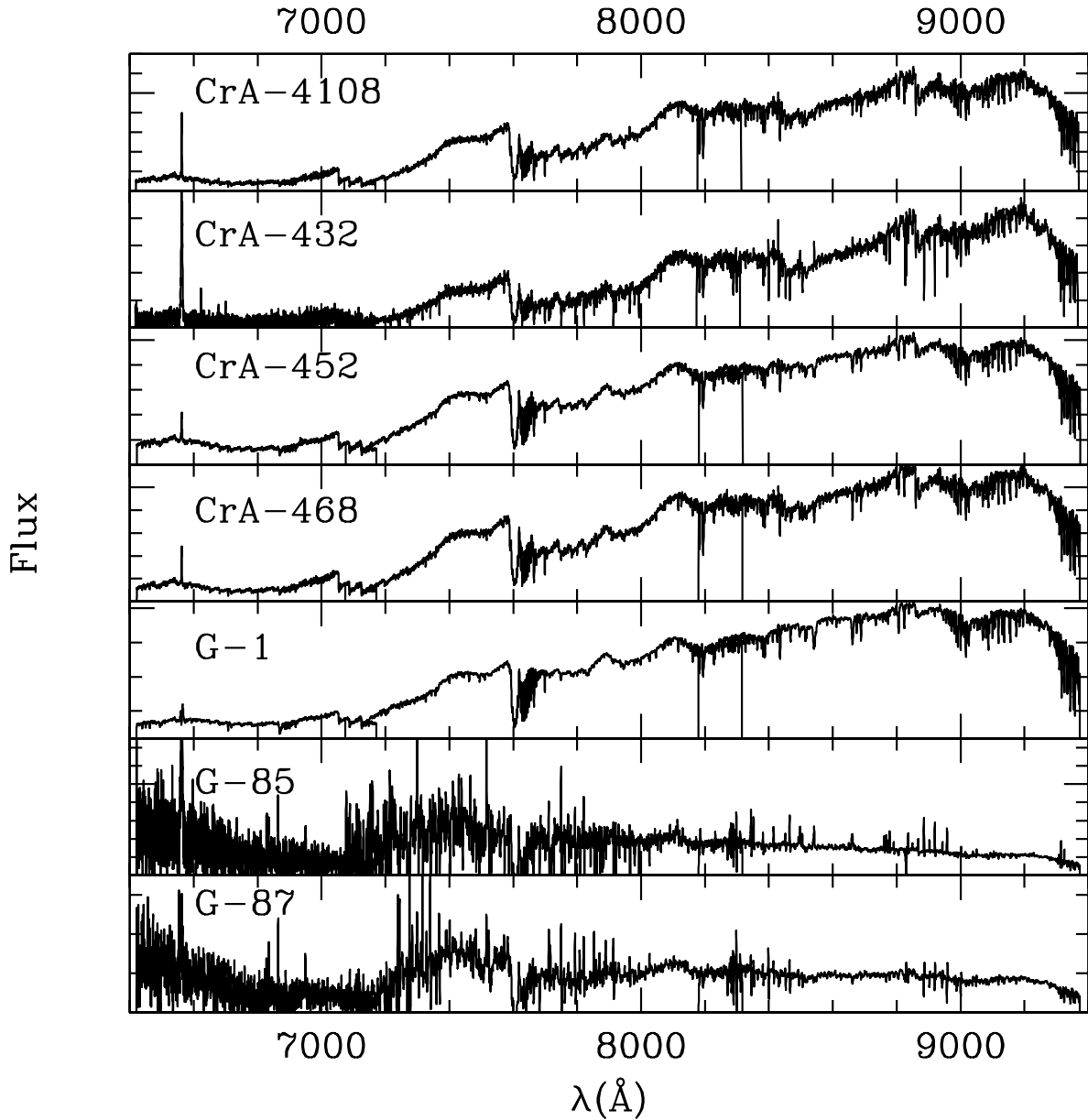
Fig. 1.— FLAMES spectra for the objects with enough S/N to derive a spectral type.
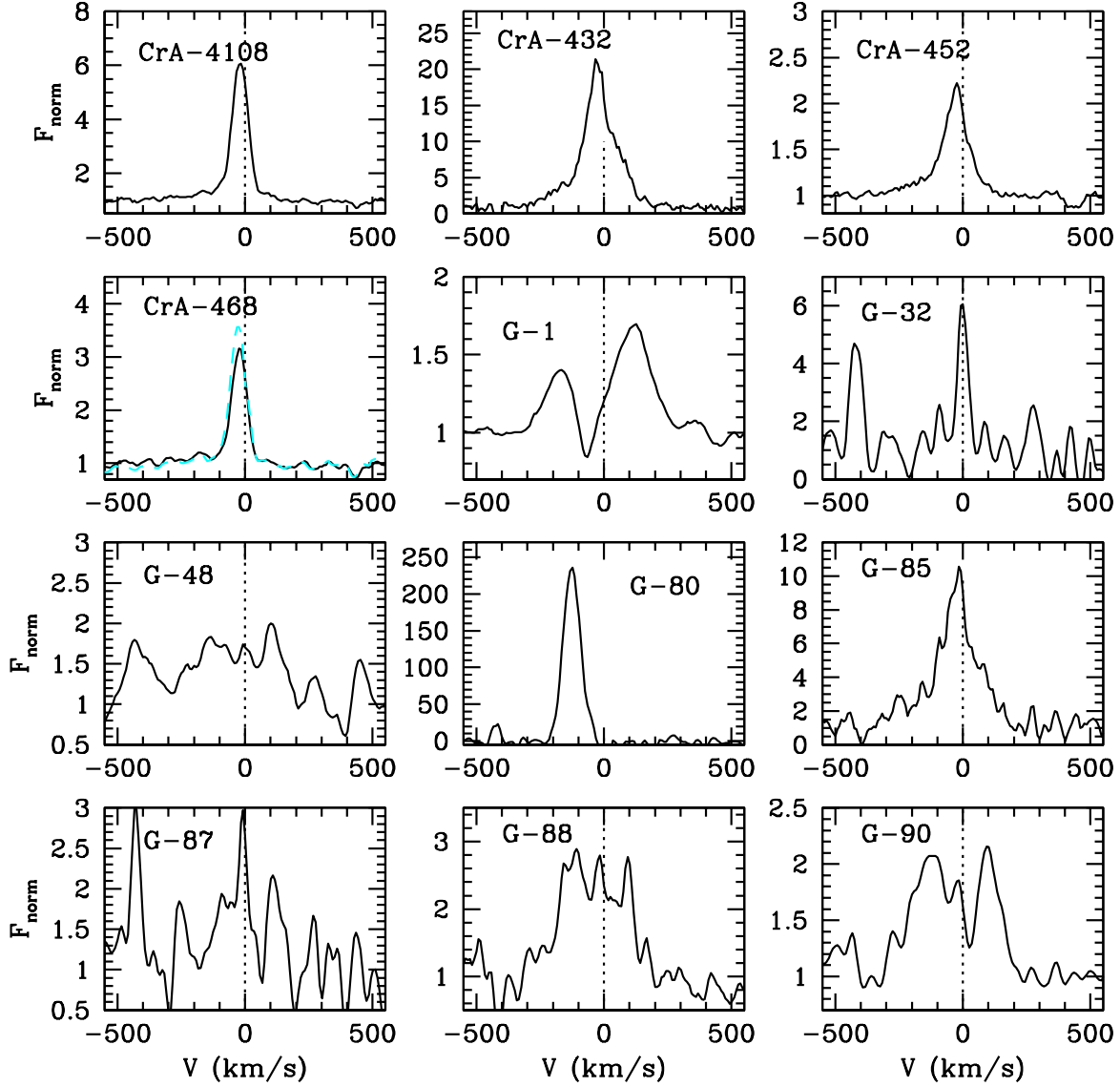
Fig. 2.— Normalized spectra in the Hα region for the detected objects. For CrA-468 (G-49), we display as a dashed cyan line our previous FLAMES spectrum (SA08).
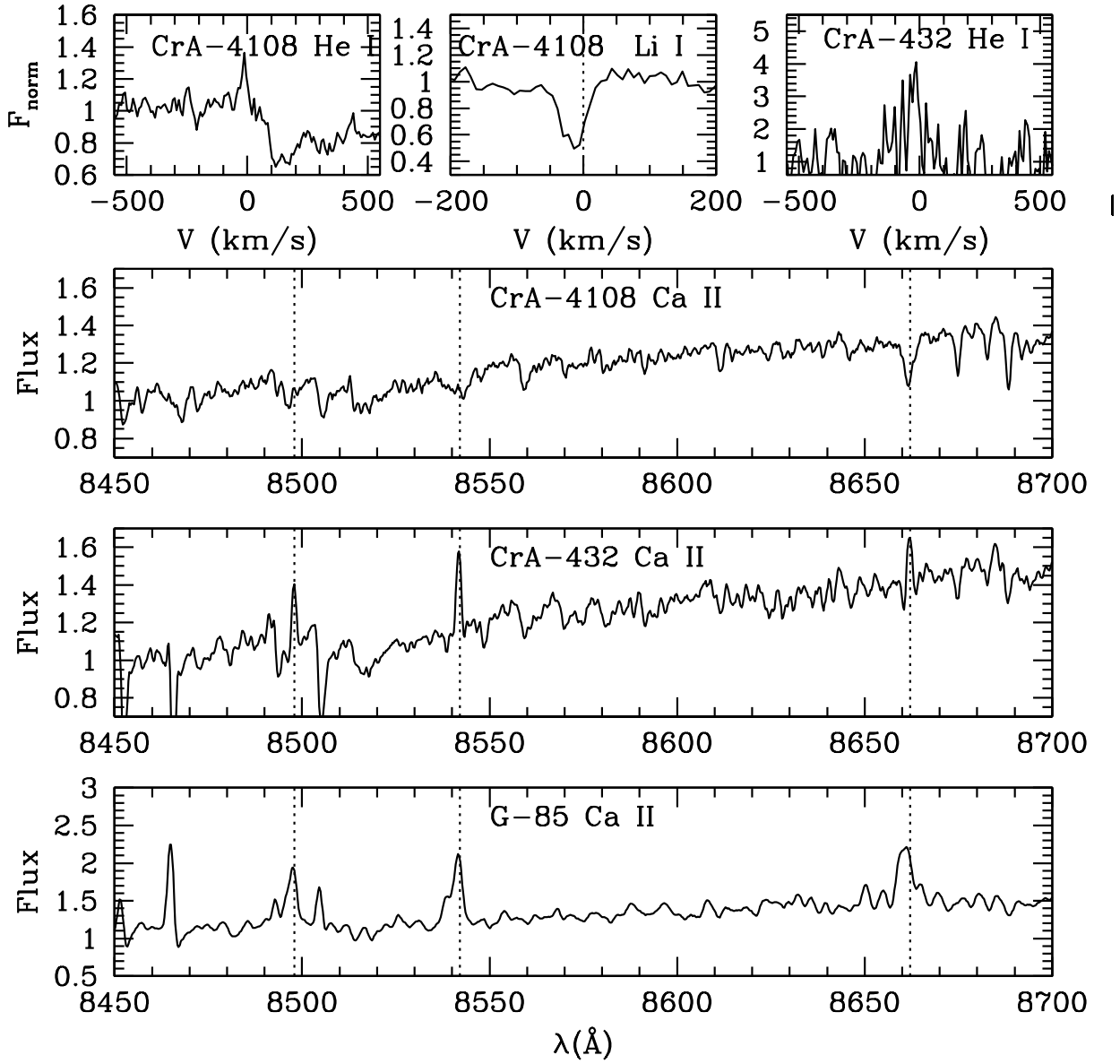
Fig. 3.— Examples of other lines detected in the spectra. The presence of He I 5875Å and the Ca II triplet in emission are indicators of accretion, Li I is a marker of youth.
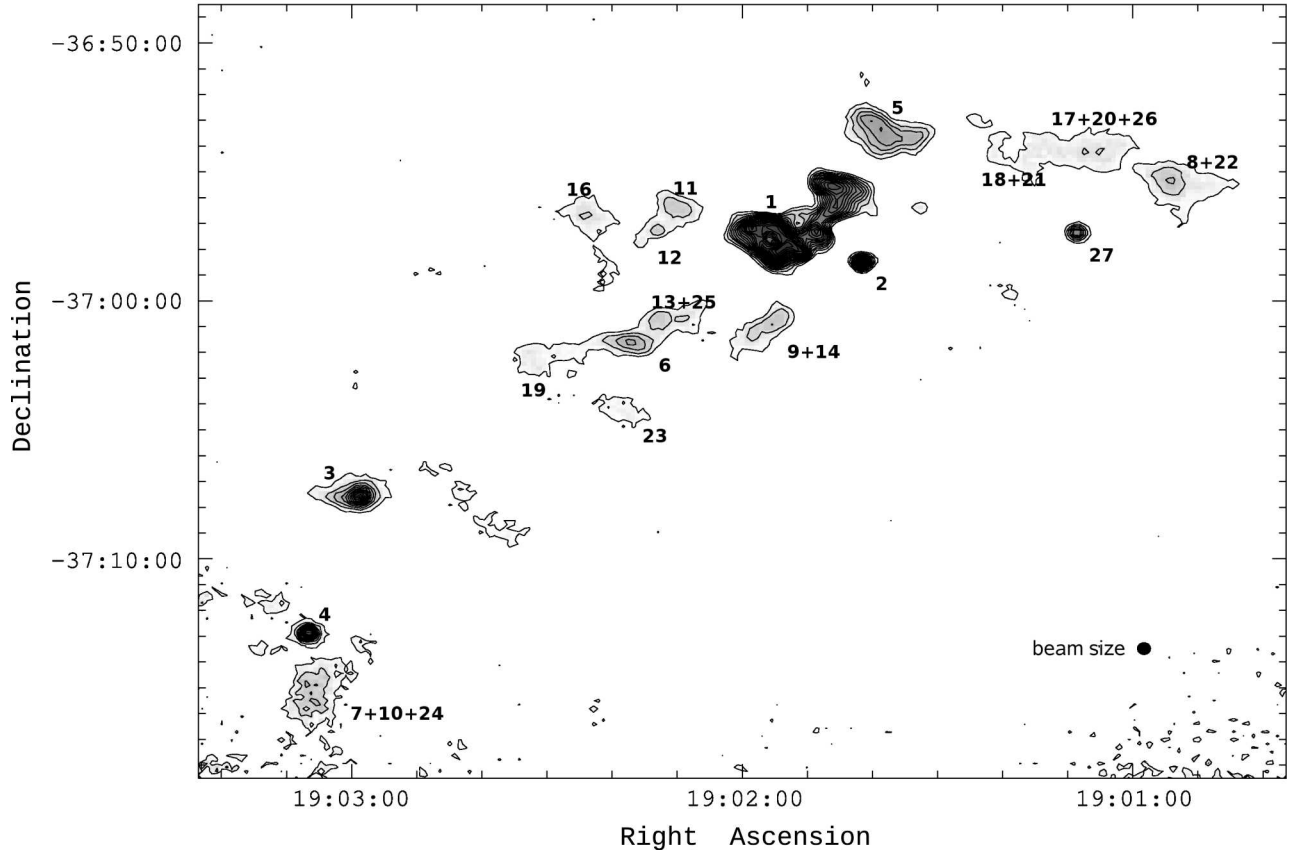
Fig. 4.— Submillimeter 870μm map obtained with APEX/LABOCA. The greyscale represent a logarithm scale between 0.030-1 Jy (approximately 3×rms). The contours are in lineal scale, from 0.030 to 1 Jy in steps of 0.050 Jy. The beam is displayed in the lower right corner. The numbers correspond to the clumps identified by Clumpfind 2D (see also Table 3). Right ascension and declination are in J2000.
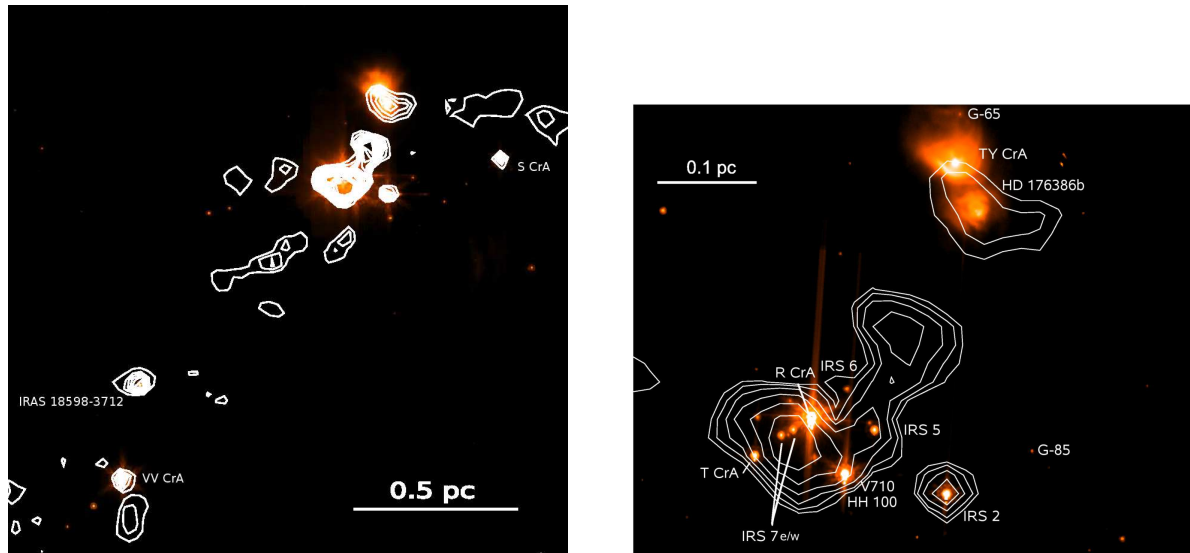
Fig. 5.— Left: LABOCA contours for the detected clumps, plotted over the MIPS 24μm image of the coronet cluster. Right: A zoom in the densest part of the nebula. The scale bars assume a distance of 170 pc.
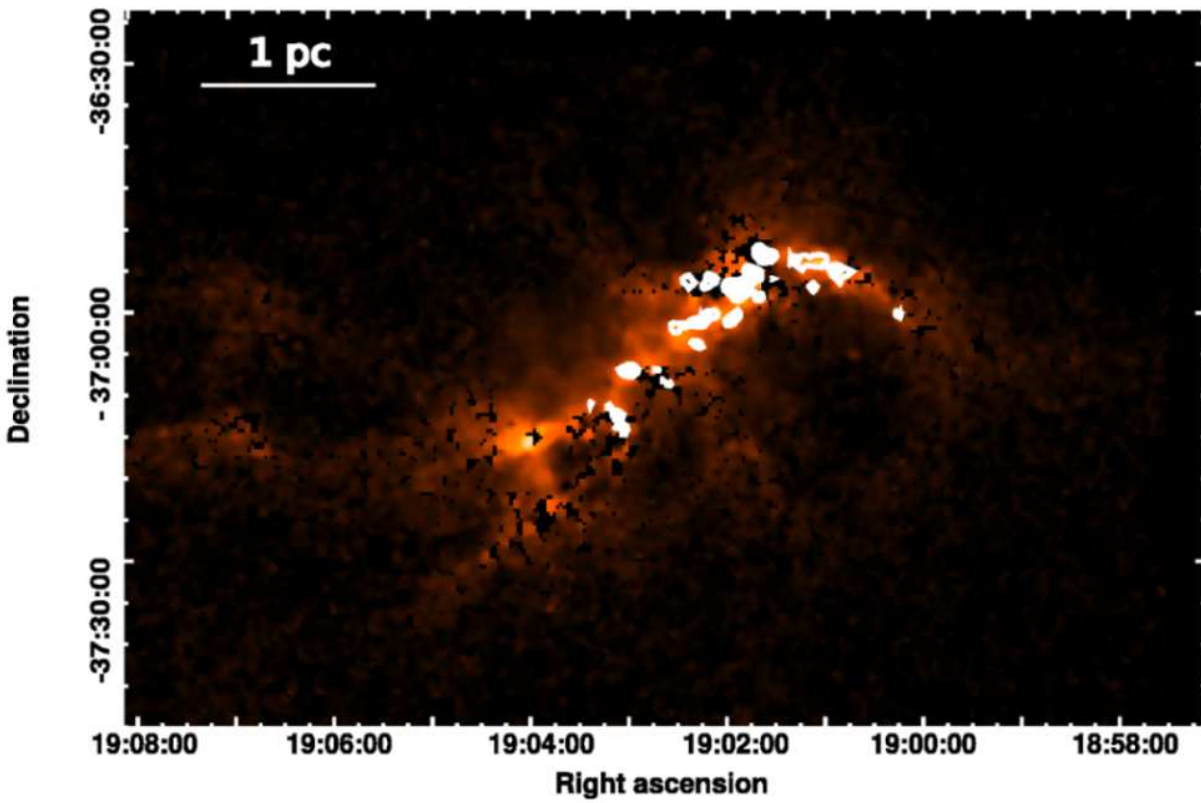
Fig. 6.— Extinction map and submillimeter structure (see text). Right ascension and declination are in J2000. The scale bar for 1 pc assumes a distance of 170 pc. The color gradient represent the extinction in a log scale from A_V=0.8 to 50 mag.
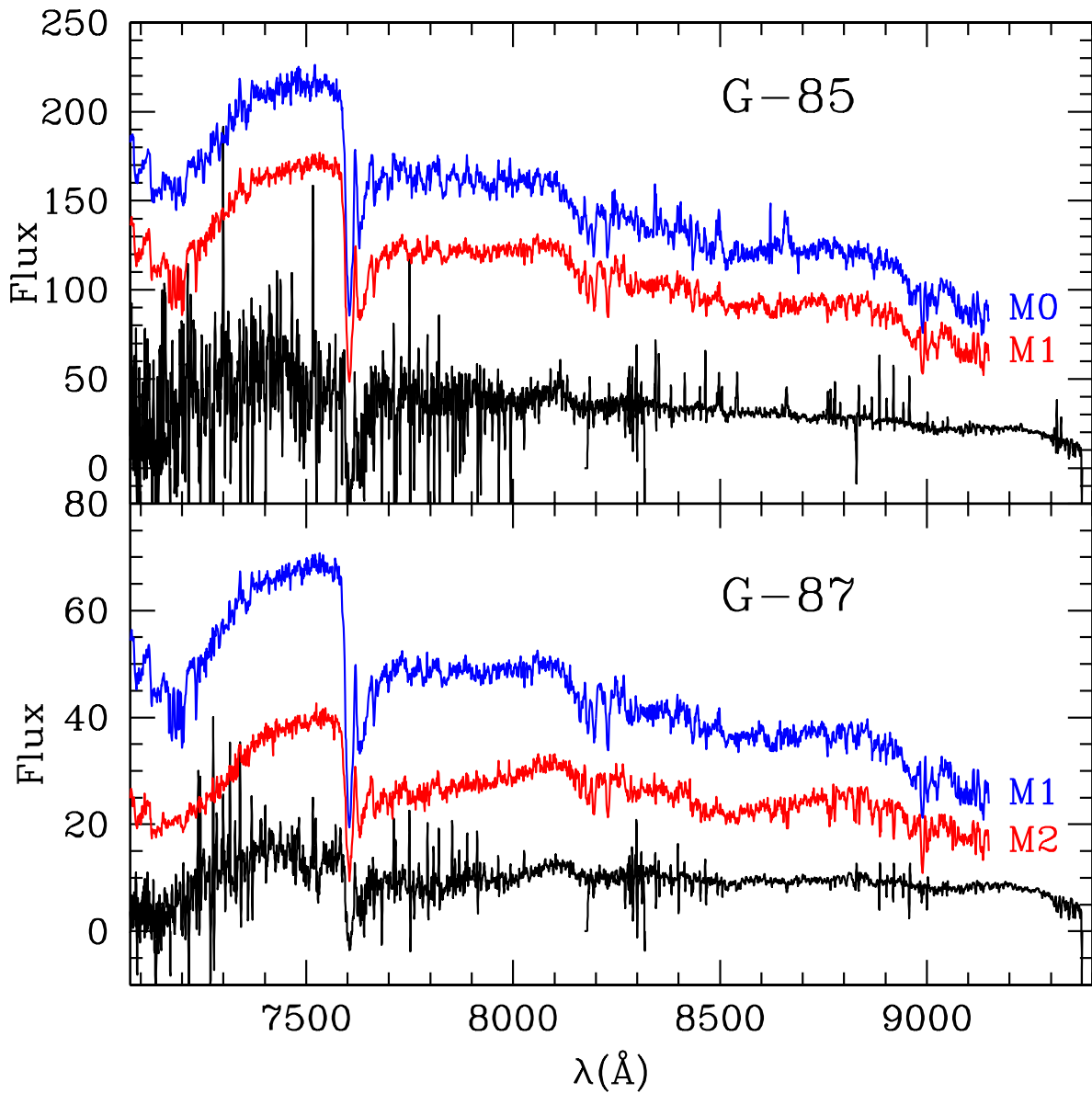
Fig. 7.— Dereddened spectra of the low S/N objects G-85 and G-87, compared to our spectral type templates.
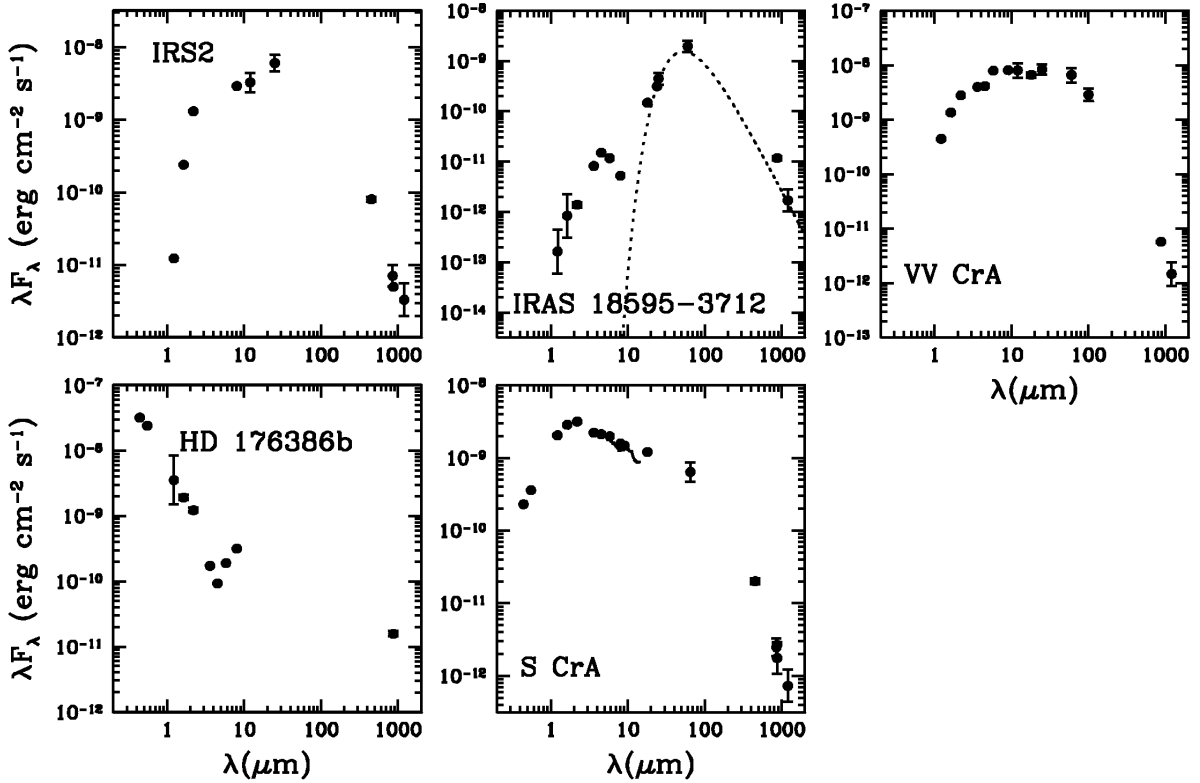
Fig. 8.— SEDs of the unresolved sources detected with APEX/LABOCA. The SEDs include the data listed in Table 5. The data for S CrA is corrected for extinction, taking A_V=0.4 mag (Currie & Sicilia-Aguilar 2011). A scaled black body emission for T=70 K is plotted as a comparison for the long wavelength emission of IRAS 18595-3712.
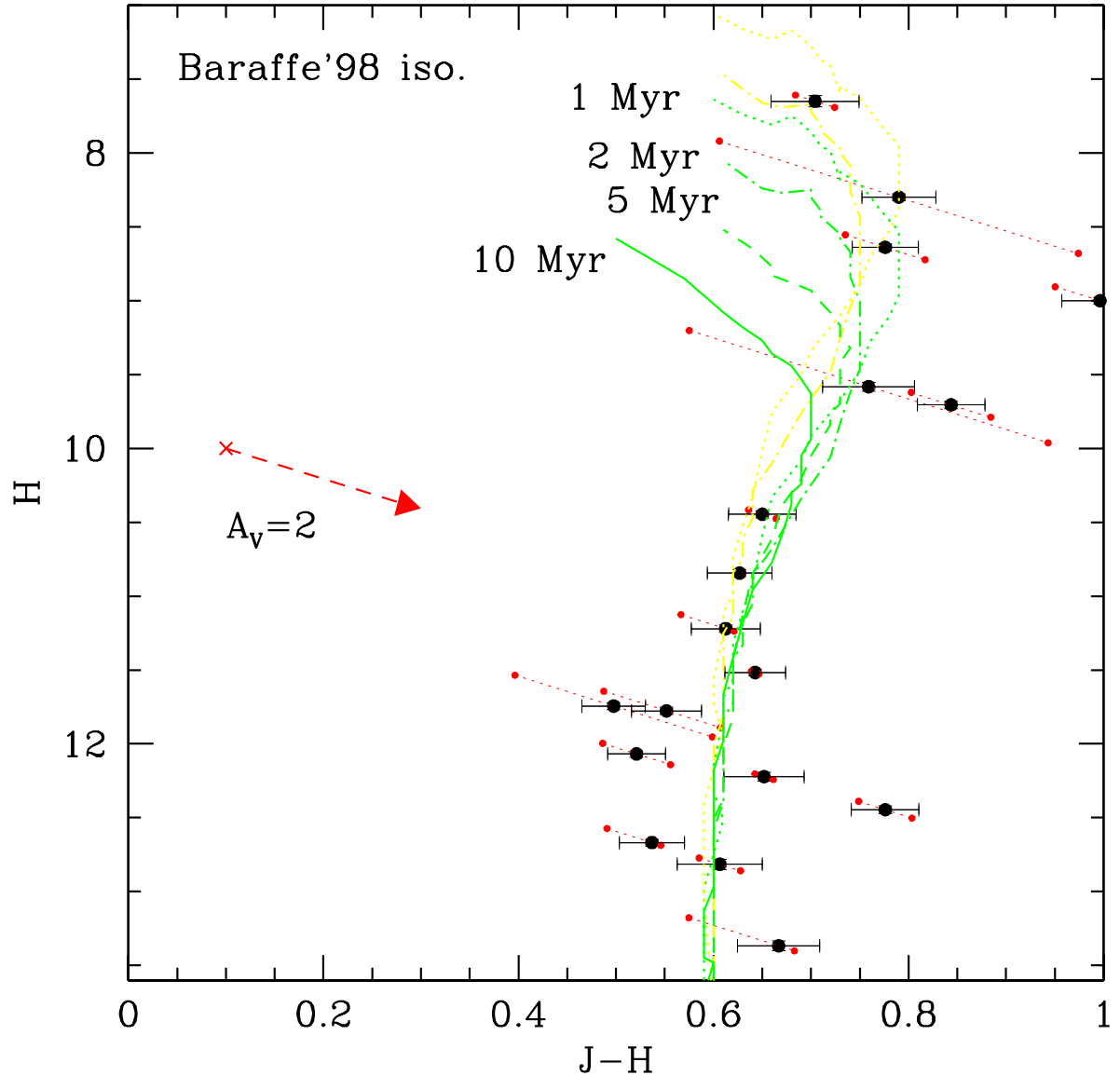
Fig. 9.— Color-magnitude diagram for the T Tauri stars in the Coronet cluster, including the new objects classified in the present work and those from our previous spectroscopy run presented in SA08. The error bars of each point include the photometry error only; in addition we add a reddening vector per data point displaying the uncertainty in the extinction/spectral type. The Baraffe et al. (1998) isochrones are displayed for two distances: 130 pc (yellow; Marraco & Rydgren 1981) and 170 pc (green; Knude & Hog 1998).